# A Nanoparticle-Based Ratiometric and Self-Calibrated Fluorescent Thermometer for Single Living Cells

**8 AUTHORS**, INCLUDING:

Yoshiaki Takei
Waseda University
4 PUBLICATIONS   66 CITATIONS

Satoshi Arai
Waseda University
30 PUBLICATIONS   247 CITATIONS

Shinji Takeoka
Waseda University
268 PUBLICATIONS   4,667 CITATIONS

Madoka Suzuki
Waseda University
47 PUBLICATIONS   331 CITATIONS

# A Nanoparticle-Based Ratiometric and Self-Calibrated Fluorescent Thermometer for Single Living Cells

Yoshiaki Takei,[†] Satoshi Arai,[‡] Atsushi Murata,[†] Masao Takabayashi,[†] Kotaro Oyama,[§] Shin'ichi Ishiwata,[‡,§,⊥] Shinji Takeoka,[†,‡,⊥,*] and Madoka Suzuki[‡,⊥,*]

[†]Department of Life Science & Medical Bioscience, Graduate School of Advanced Science & Engineering, Waseda University, 2-2 TWIns, Wakamatsu-cho, Shinjuku-ku, Tokyo, 162-8480 Japan, [‡]Waseda Bioscience Research Institute in Singapore, Waseda University, 11 Biopolis Way, #05-01/02, Helios, Singapore, 138667 Republic of Singapore, [§]Department of Physics, Graduate School of Advanced Science and Engineering, Waseda University, 3-4-1 Okubo, Sinjuku-ku, Tokyo, 169-8555 Japan, and [⊥]Organization for University Research Initiatives, Waseda University, #304, Block 120-4, 513 Wasedatsurumaki-cho, Shinjuku-ku, Tokyo, 162-0041 Japan

**ABSTRACT** The homeostasis of body temperature and energy balance is one of the major principles in biology. Nanoscale thermometry of aqueous solutions is a challenging but crucial technique to understand the molecular basis of this essential process. Here, we developed a ratiometric nanothermometer (RNT) for intracellular temperature measurement in real time. Both the thermosensitive fluorophore, $\beta$-diketonate chelate europium(III) thenoyltrifluoroacetonate, and the thermoinsensitive fluorophore, rhodamine 101, which was used as a self-reference, are embedded in a polymeric particle that protects the fluorophores from intracellular conditions. The ratiometric measurement of single RNT spots is independent of the displacement of the RNT along the $z$-axis. The temperature is therefore determined at the location of each RNT under an optical microscope regardless of the dynamic movement of living cells. As a demonstration of the spot-by-spot intracellular thermometry, we successfully followed the temperature change in individual RNT spots in a single cell together with the $Ca^{2+}$ burst induced by the $Ca^{2+}$ ionophore ionomycin. The temperature increases differently among different spots, implying heterogeneous heat production in the cell. We then show that, in some spots, the temperature gradually decreases, while in others it remains high. The average temperature elevation within a cell is positively correlated to the increase in $Ca^{2+}$, suggesting that the activity and/or number of heat sources are dependent on the $Ca^{2+}$ concentration.
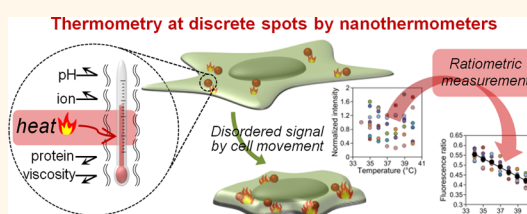
**KEYWORDS:** $Ca^{2+}$-ATPase · fluorescent nanoparticle · polymer nanoparticle · ratiometry · rhodamine 101 · thermogenesis · thermometry

Thermometry at discrete spots by nanothermometers

Heat production from within is a key process in endothermic animals in order to maintain viability, but the details of local heat production at the level of individual cells or organelles still remain elusive. Fluorescence imaging has the potential to be a powerful method of intracellular thermometry owing to its high spatiotemporal resolution. For this purpose, various types of fluorescent nanothermometers have recently been developed.[1,2] These are based on quantum dots,[3−5] fluorescent proteins,[6] $Ln^{3+}$-based nanoparticles,[7,8] polymer dots,[9] polymer nanogels,[10,11] organic−inorganic hybrid nanoparticles,[12−15] and polymer nanoparticles.[16] Thermometry measuring the fluorescence spectrum[4] or the fluorescence lifetime[11,15] of fluorescent nanothermometers is independent

of changes in the concentration of fluorophores in each nanothermometer and of focus drift. However, these methods require a certain period of time to complete $x−y$ scanning to obtain a sufficient number of photons per pixel in each spot. The measurement time increases as the number of spotted areas increases. These methods are therefore only suitable for situations where the single nanothermometers of interest do not move, or move very slowly, during the time required for measurement.

Ratiometric measurements are dependent on the fluorescence intensities.[5,7−9,12−14] Although this can negate changes in the concentration of fluorophores and the focus, the fluorescence intensity can be altered by environmental parameters. Furthermore, the readout signal, as well as the ratio of the two
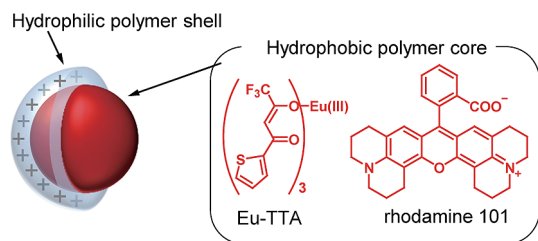
**Figure 1. Schematic illustration of ratiometric fluorescent nanothermometers.** Thermosensitive (Eu-TTA: $\lambda_{Ex}$ = 341 nm, $\lambda_{Em}$ = 612 nm) and thermoinsensitive (rhodamine 101: $\lambda_{Ex}$ = 560 nm, $\lambda_{Em}$ = 587 nm) fluorophores are embedded in the hydrophobic (PMMA) core. A hydrophilic polymer shell composed of positively charged PAH isolates the core from the exterior environment.

signals, deteriorates due to the fluctuation in fluorescence intensity produced by the light source, the optical setup, and the detector. Nonetheless, the measurement of the fluorescence intensity still maintains the advantage that spatial information in the $x-y$ plane can be obtained in a single camera frame regardless of the number of spots of interest and with a sufficiently high temporal resolution using a relatively simple optical setup. The signal-to-noise ratio can be improved by averaging camera frames if necessary. These features can be harnessed using a combination of different optical methods and in doing so allow for a variety of parameters to be quantified at the same time.

In order to understand activity-coupled heat production at the single-cell level, it is necessary to measure local heat production together with cellular activities, such as $Ca^{2+}$ dynamics.[17] In this paper, we report a new nanothermometer modified from our one-color particle previously reported.[16] This polymer-based nanoparticle works as a ratiometric nanothermometer (RNT). Ratiometric measurement improves the accuracy of intensity-based thermometry, as it is capable of compensating for physical errors, such as the position drift of the particles caused by the active motion of living cells. Furthermore, each RNT spot provides a readout of the temperature. The RNT contains both thermosensitive europium(III) thenoyltrifluoroacetonate (Eu-TTA) and thermoinsensitive rhodamine 101, which serves as an internal reference, which are embedded in a poly(methyl methacrylate) (PMMA) polymer nanoparticle that is further covered by poly-(allylamine) hydrochloride (PAH) (Figure 1). These polymers serve as barriers protecting the fluorophores from the intracellular environment, while preserving the thermosensitivity at the core of the particle. We evaluated this nanothermometer in terms of its insensitivity to various intracellular conditions and the effect of displacement along the $z$-axis. Finally, using ratiometric measurements combined with fluorescence $Ca^{2+}$ imaging, we successfully tracked the heat production correlated with cytosolic $Ca^{2+}$ concentration by single RNT spots in single living HeLa cells.

## RESULTS AND DISCUSSION

RNTs were prepared *via* an emulsion diffusion—evaporation method.[18] The diameter of the core containing fluorophores was 99.4 ± 30.7 nm [mean ± standard deviation (SD), $n$ = 157] estimated from transmission electron microscope images. The mean diameter determined by scanning electron microscopy was 140 ± 59.9 nm (mean ± SD, $n$ = 336). The surface charge of the RNTs was designed to be positive [40.3 ± 1.84 mV (mean ± SD), as measured by laser Doppler velocimetry in deionized water] by coating the core with cationic PAH, which facilitates cellular uptake. The hydrodynamic diameter including the PAH hydrophilic phase was centered at 143 ± 36.2 nm (mean ± SD) as determined by dynamic light scattering.

We chose the fluorophores Eu-TTA and rhodamine 101 for four key reasons: (i) both fluorophores can successfully be embedded in a core composed of PMMA, (ii) excitation and emission spectra of both fluorophores can be well separated from that of the fluorescent $Ca^{2+}$ indicator, Fluo-4, (iii) Eu-TTA has a large Stokes shift and its excitation spectrum is far from that of rhodamine 101, and (iv) the fluorescence intensity of Eu-TTA responds significantly to temperature changes in a reversible manner, whereas the fluorescence from rhodamine 101 is constant within the range we studied (Figure 2A). The fluorescence ratio of these two fluorophores (Eu-TTA/rhodamine 101, calculated from the peak intensities of Eu-TTA and rhodamine 101 at 612 and 587 nm, respectively) decreases linearly as the temperature is increased from 26 °C to 40 °C (Figure 2B).

In living cells, the environmental conditions such as ionic strength,[19] pH,[20−22] protein concentration, and viscosity[23,24] are not constant in space and time. Fluorescent thermometers are usually sensitive not only to temperature but also to these other environmental parameters. In our RNTs, the fluorescence ratio (Eu-TTA/rhodamine 101, where Eu-TTA and rhodamine 101 were excited at 360 ± 20 and 530 ± 40 nm, respectively, and collected at 590 ± 35 and 530 ± 40 nm, respectively) as well as their thermal sensitivity did not change in the following conditions: pH of 4−10 (Figure 2C, SD = 0.2 °C), ionic strength of 0−500 mM (Figure 2D, SD = 0.3 °C), protein concentration of 0−45 wt % (Figure 2E, SD = 0.7 °C), viscosity of 1−220 cP (Figure 2F, SD = 0.4 °C). It was also confirmed that the fluorescence ratio of RNTs was insensitive to oxygen level (Figure S4A, SD = 0.6 °C) and stable for at least 12 h (Figure S4B, SD = 0.4 °C in water and SD = 0.5 °C). These results indicate that the hydrophobic core and hydrophilic shell effectively protect fluorophores in the core from the surrounding environment. We therefore conclude that the RNTs developed
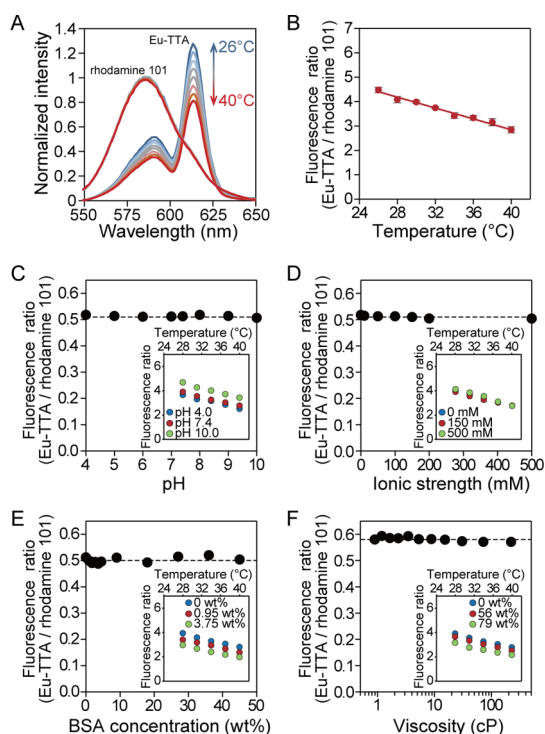
**Figure 2.** Sensitivity of RNTs to various parameters determined in a cuvette. (A) Fluorescence spectra of Eu-TTA and rhodamine 101 measured by a spectrophotometer at every 2 °C increase from 26 °C to 40 °C. Eu-TTA and rhodamine 101 were excited at 340 and 530 nm, respectively. (B) Fluorescence ratio (Eu-TTA/rhodamine 101) calculated from the peak intensities of Eu-TTA and rhodamine 101 at 612 and 587 nm, respectively, at various temperatures. The slope of the linear fit (solid line) was −0.108/°C. Error bars, SD ($n = 4$). (C−F) Fluorescence ratio (Eu-TTA/rhodamine 101, where Eu-TTA and rhodamine 101 were excited at 360 ± 20 and 530 ± 40 nm, respectively, and collected at 590 ± 35 and 530 ± 40 nm, respectively, by a microplate reader) at 28 °C in (C) phosphate buffer (pH 4−10), 0.51 ± 0.0037 (mean ± standard deviation, calculated from all data points), (D) KCl solution (KCl 0−500 mM), 0.51 ± 0.0051, (E) BSA solution (BSA 0−45 wt %), 0.50 ± 0.011, and at 25 °C in (F) viscous solution [glycerol/PBS 0−92 wt % ,which corresponds to 1−220 cP at 25 °C[38]], 0.58 ± 0.0077. Broken lines indicate $y = 0.51$, $y = 0.51$, $y = 0.50$, and $y = 0.58$ in (C) to (F), respectively. (Inset) Temperature-dependent decrease of the fluorescence ratio in the respective exterior environment measured by a spectrophotometer. The slopes were −0.091/°C, −0.093/°C, and −0.103/°C at pH 4.0, pH 7.4, and pH 10.0, respectively in (C), −0.108/°C, −0.093/°C, and −0.116/°C at KCl 0 mM, 150 mM, and 500 mM, respectively in (D), −0.093/°C, −0.087/°C, and −0.083/°C at BSA 0 wt %, 0.95 wt %, and 3.75 wt %, respectively, in (E), and −0.093/°C, −0.094/°C, and −0.080/°C at glycerol 0 wt %, 56 wt %, and 79 wt %, respectively, in (F).

here are capable of determining the temperature without being disturbed by multiple environmental parameters.

Next, we examined the properties of RNT under the optical microscope. Although AFM images support the presence of single RNT particles, RNT clusters were also observed on the glass coverslip in the presence of 10% FBS (Figure S1, E and G). As we could not eliminate the possibility to observe RNT clusters under an optical microscope, we refer to the fluorescence images of RNTs as RNT spots.

We first evaluated the influence of unfocusing by shifting the objective lens along the z-axis while observing RNTs attached to the glass surface. The fluorescence intensities of both Eu-TTA (excited by 354−366 nm and collected at 570−625 nm) and rhodamine 101 (exited by 535−555 nm and collected at 601−657 nm) were maximal at $z = 0$, where the RNT was in focus, and decreased as the RNT was defocused both up and down the z-axis. The ratio, however, remained constant (Figure 3A), demonstrating the advantage of ratiometric measurement.

We then assessed RNTs in a cancer cell line (HeLa) to test their properties in living cells. RNTs displayed low toxicity to HeLa cells at the concentration examined (ca. 90% viability at 0.015 mg/mL, Figure S5). The localization of RNTs was specific to endosomes (Figure 3B). A few RNT spots were observed in the cytosol, but they did not co-localize with any other organelles. These observations suggest that, owing to the surface positive charge, most of the RNTs were attached to the plasma membrane and then taken up via endocytosis as we observed previously.[16]

We further evaluated the ability of single RNT spots to measure the temperature by comparing the temperature-dependent fluorescence intensity and the ratio of RNTs outside and inside a cell in the same field of view (Figure 3C and Movie S1). The linear decrease in the fluorescence intensity of Eu-TTA in RNTs was clearly observed outside the cell (Figure 3D), whereas the signals of RNTs in the cell were disordered (Figure 3F). This was due to the displacement of RNTs along the z-axis caused by cell movement. In direct contrast to these results, the ratiometric measurement appropriately compensated for the position drift within the cell. We were able to plot the fluorescence ratio against the temperature both outside (Figure 3E) and inside (Figure 3G) the cell. The fluctuation of data points inside the cells away from a fitted line was within the range of measurement error (Figure 3G). The thermal sensitivity of RNTs in the cell was therefore confirmed to be the same as RNTs on the glass surface.

Eu-TTA can be problematic for biological applications due to its toxic excitation spectrum peaking within the UV range. Its low photostability is another drawback. These problems were mitigated by shortening the excitation period for Eu-TTA and by calibrating the photobleaching. The temperature measurement was accurate with a SD of 0.0231, or 1.0 °C with 10 ms exposure time for Eu-TTA (Figure S7C). We also concluded that the intracellular temperature synchronized with the exterior medium temperature from 34 to 40 °C in the case of slow heating (Table S1).

Care should be taken when the ratio values are compared in different apparatus such as the fluorescent spectrophotometer and the fluorescence optical microscope. The dual-excitation two-color ratio imaging as employed in our RNT excites two fluorophores
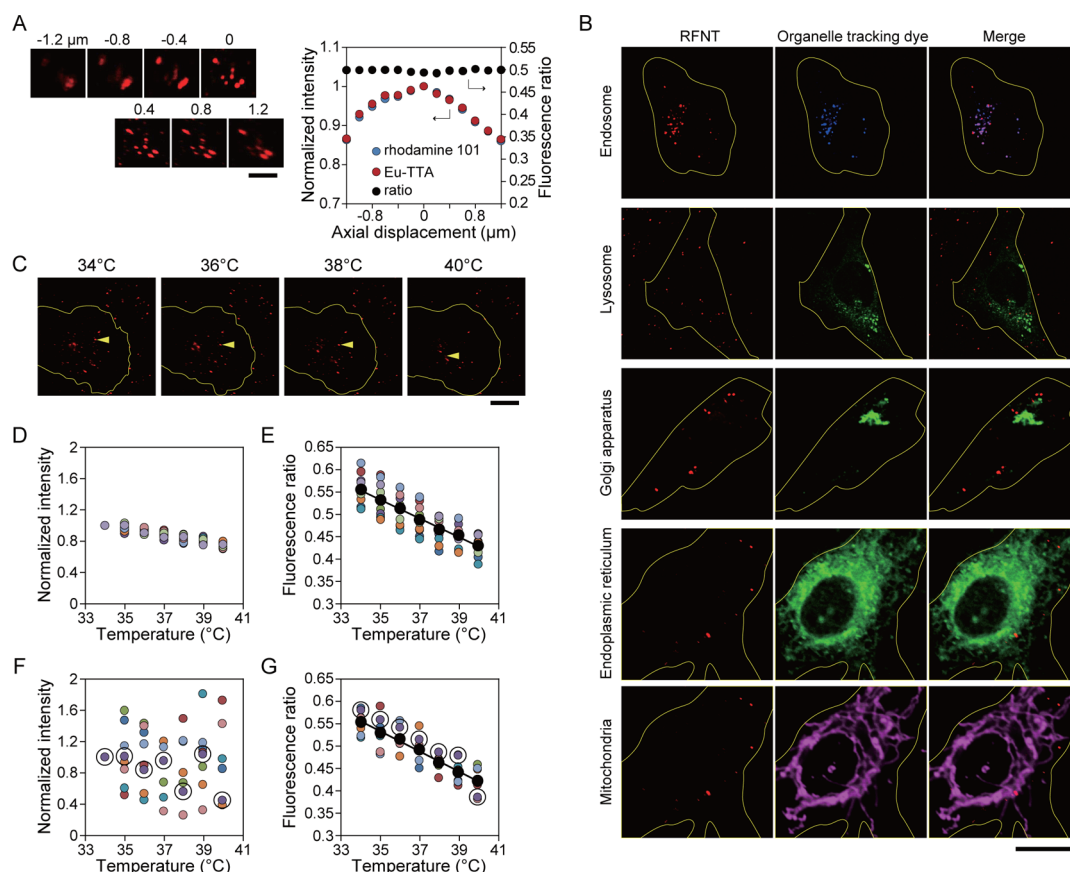
**Figure 3. Specifications of single RNT spots determined under the optical microscope. (A)** Focus-independent fluorescence ratio of single RNT spots. (Left) Epifluorescence images of RNTs (rhodamine 101) attached to a glass surface. The numbers above each image indicate the z-position of the focus. $z = 0$ at the glass surface. Scale bar, 20 $\mu$m. (Right) Fluorescence intensities of both rhodamine 101 (blue, excited by 535−555 nm and collected through 601−657 nm) and Eu-TTA (red, excited by 354−366 nm and collected through 570−625 nm) approached the maximum at $z = 0$ and decreased with defocusing, whereas the fluorescence ratio (black, Eu-TTA/rhodamine 101) was always constant. **(B)** Location of RNTs in living HeLa cells. From left to right columns: confocal fluorescence microscopy images of rhodamine 101 in RNTs, tracking dyes for the organelles indicated on the left and their merging. Periphery of the cell is indicated by the yellow line. Scale bar, 10 $\mu$m. **(C−G)** Measurement of the temperature inside and outside living HeLa cells. **(C)** Epifluorescence images of rhodamine 101 in RNTs at various temperatures indicated above. Periphery of the cell is indicated by the yellow line. Yellow arrowhead indicates the RNT spot shown in F and G by circled plots. Scale bar, 20 $\mu$m. Fluorescence intensities of RNTs (Eu-TTA) outside the cell decreased uniformly as the temperature increased **(D)**, while those inside the cell showed extensive drift because of the movement of the cell **(F)**. Ratiometric measurement (Eu-TTA/rhodamine 101) properly indicated the temperature both outside **(E)** and inside **(G)** the cell. Plots in the same color code as **(D)** and **(E)**, and **(F)** and **(G)**, respectively, were obtained from the same single RNT spot. Black plots: the average values at each temperature. Circled plots: the RNT spot shown in **(C)** with a yellow arrowhead. The slope of the linear fit for the average values (black lines) was −0.0206/°C in **(E)** and −0.0221/°C in **(G)**.

with two lights to measure two emissions. Then the ratio can be determined by the two excitation lights and the two emission lights. By changing the light intensities of the two excitation bands, we can adjust the emission intensities of Eu-TTA and rhodamine 101 independent of each other. The absolute value of the ratio (Eu-TTA/rhodamine 101) is, therefore, adjustable in each apparatus. The apparent temperature sensitivity in a unit of "ratio/°C" will vary among setups as we measured in the fluorescence photometer (about −0.1/°C in Figure 2) and the fluorescence microscope (about −0.02/°C in Figure 3). It is, however, an advantage that we are able to optimize the configurations of observations separately for each fluorophore.

Finally, as a demonstration of our RNT as an intracellular thermometer, we set out to measure temperature

change and Ca$^{2+}$ dynamics at the same time in single, ionomycin-stimulated HeLa cells (Figures 4, S9, and S10 and Movie S2). We have previously shown that Ca$^{2+}$-coupled heat production, induced by the Ca$^{2+}$-ionophore ionomycin, can be detected at the surface of a HeLa cell.[25] Yang et al. subsequently reported on heat production induced by ionomycin inside NIH3T3 cells.[4] We selected the stimulation conditions such that (i) the relatively strong Ca$^{2+}$ burst was induced immediately after the application of ionomycin (Figure 4A and B, center, top) and (ii) the cells were greatly stressed (Figure 4A and Movie S2, after $t = 30$ s), resulting in cell death in most cases (cf. Figure 4A and Movie S2, after $t = 140$ s). After the Ca$^{2+}$ burst, the fluorescence ratio of RNT decreased, which was distinguishable from photobleaching (Figure 4B, center, middle). This strongly
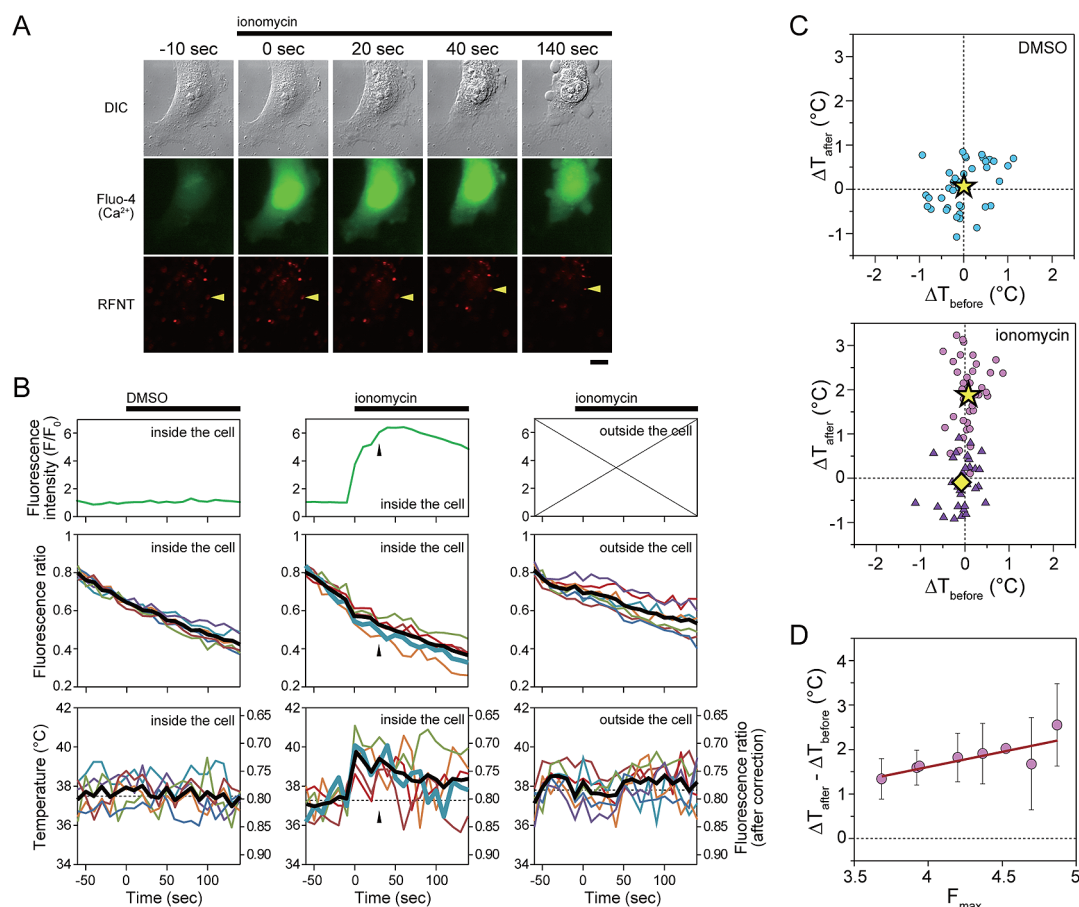
**Figure 4. Heterogeneous temperature dynamics coupled with chemically induced Ca$^{2+}$ burst in HeLa cells.** (A) Time-lapse imaging of the differential interference contrast (DIC) images (top) and the fluorescence images of Fluo-4 (middle) and rhodamine 101 in RNTs (bottom). Ionomycin Ca$^{2+}$ complex was applied to the cell between $t = -10$ and 0 s. The cell began to shrink at $t = 30$ s. Yellow arrowhead: the RNT spot shown in (B), center, with a thick cyan line. Scale bar, 10 $\mu$m. (B) Typical time courses of the normalized fluorescence intensity of Fluo-4 (top), the fluorescence ratio of RNTs (Eu-TTA/rhodamine 101, middle), and the temperature (bottom) measured either inside (left and center) or outside (right) the cell. Optical filters used were the same as in Figure 3C−G. Fluo-4 intensity was measured as the average fluorescence intensity from the whole cell area and normalized in each cell ($F/F_0$) using the average value before the application of DMSO or ionomycin ($F_0$). The photobleaching of each RNT spot (middle) was canceled out by fitting the time course of the RNT between $t = -60$ s and $-10$ s with a single-exponential curve. The temperature was then calculated from the calibration data separately obtained from RNTs on a glass surface (Figure S8). DMSO (left) or ionomycin (center and right) was applied to the cell as indicated on top. The moments when the cells began to deform are indicated by arrowheads. Thick black lines: the average. Dotted lines: the average before stimulation (bottom). Thick cyan line: the RNT spot shown in (A) with a yellow arrowhead. Data on the center and right were analyzed from the original images of (A). (C) Relationship between the temperature differences before ($\Delta T_{before}$) and after ($\Delta T_{after}$) the application of either DMSO (upper, $n = 43$ spots in 7 cells) or ionomycin (lower, $n = 38$ and 33 spots inside and outside of 8 cells, respectively). $\Delta T_{before}$ and $\Delta T_{after}$ are the average from $-60$ to $-20$ s and from 10 to 50 s, respectively. Circles and yellow stars: RNTs inside of cells. Triangles and the yellow diamond: RNTs outside of cells. Stars in upper and lower panels are plotted at (0.0 $\pm$ 0.5 °C, 0.1 $\pm$ 0.5 °C) and (0.1 $\pm$ 0.3 °C, 1.9 $\pm$ 0.8 °C), respectively (mean$_{before}$ $\pm$ SD$_{before}$, mean$_{after}$ $\pm$ SD$_{after}$). The diamond is plotted at ($-0.1 \pm 0.3$ °C, $-0.1 \pm 0.5$ °C). (D) The relationship between the maximum fluorescence intensity of Fluo-4 before cell deformation ($F_{max} = (F - F_0)/F_0$) and the temperature difference between before and after the application of ionomycin ($\Delta T_{after} - \Delta T_{before}$) measured inside cells. Error bars indicate the SD from more than five data points. $N = 8$ cells. Solid line shows the linear fit, $y = 0.71x - 1.23$, $R^2 = 0.67$.

suggests that the observed signals in RNTs indicate the heat production at each of their specific locations. In the representative data shown here (Figure 4B, center, bottom), the intracellular temperature was approximately 37 °C before ionomycin addition. It rose to approximately 39 °C following ionomycin treatment, which preceded the shrinking of the cell at around $t = 30$ s. During shrinkage, some RNT spots maintained a high temperature while others showed a decrease in temperature (Figure S9). The latter case probably

indicates the end stage of heat production originally induced by ionomycin or the end of cellular activities due to cell death. The temperature increase ($\Delta T$) was sometimes observed with a time delay, as we previously observed;[25] however, there was a variance of 10.8 $\pm$ 12.8 s (mean $\pm$ SD) in the increase of the fluorescence intensity of Fluo-4 (Figure S10). The average $\Delta T$ five frames after heat generation, $\Delta T_{after}$, was 1.9 $\pm$ 0.8 °C (mean $\pm$ SD) in all measurements (Figure 4C, lower). The heterogeneous heat production

in degrees, space, and time was therefore successfully detected in each cell. There was a positive correlation in the maximum fluorescence intensity of Fluo-4 before cell deformation and the temperature difference between $\Delta T_{after}$ and the average $\Delta T$ five frames before the heat production, $\Delta T_{before}$ (Figure 4D). No heat production was detected in control measurements when a PBS/DMSO solution was added instead of ionomycin (Figure 4B, left, C, upper, and Figure S9A) or in RNTs outside cells (Figure 4B, right, C, lower, and Figure S9C).

The signal distribution of the intracellular temperatures reported by intracellular RNTs (Figure 3G) was similar to the signals from extracellular RNTs at each temperature (Figure 3E). The SD was ~1 °C in both situations when Eu-TTA was excited for 10 ms. With an exposure time of 20 ms, the signal-to-noise ratio was improved. The intrinsic error evaluated from the SD of RNTs outside the cell was 0.5 °C (Figure 4C, bottom, triangles and a diamond). The intracellular temperatures again showed a similar distribution before DMSO (SD = 0.5 °C, Figure 4C, upper) or ionomycin (SD = 0.3 °C, Figure 4C, lower, circles and a star) was applied, and also after DMSO was applied (SD = 0.5 °C, Figure 4C, upper, $F = 1.100\,657 < F_{0.025,\ 42,\ 42} = 1.670\,971$ examined by $F$-test at the 0.05 significance level). These distributions were attributed to the varying thermal properties among RNTs. The addition of ionomycin broadened the intracellular temperature distribution significantly to 0.8 °C (Figure 4C, lower, $F = 2.309\,283 > F_{0.025,\ 37,\ 42} = 1.691\,709$ examined by $F$-test at the 0.05 significance level). This increased distribution in intracellular temperature suggests heterogeneous local heat production in single cells. Yang et al. recently reported a similar trend in NIH3T3 cells as detected by the spectrum shift of Q-dots during the ionomycin-induced $Ca^{2+}$ burst.[4] The average $\Delta T_{after}$, +1.9 °C, is consistent with their measurements (+1.84 °C). Their results, however, showed a large number of $\Delta T_{after}$ points higher than 2 °C. There are a few possible explanations for this. First, the distribution of the thermal properties of the Q-dots they studied was significantly larger than that of ours, as they have discussed. Although the average value of Q-dot peak wavelength correlates with the temperature, its distribution among Q-dots at each temperature was broad. When determining the temperature, we decreased the distribution among RNTs by setting a fluorescence intensity threshold (Figure S7). Second, although the protocol for the $Ca^{2+}$ burst was quite similar, the effects on the cells could be different. As we observed in Figure 4, the variety in $Ca^{2+}$ dynamics leads to a variety in heat production. Third, the specific location of the nanothermometer within the cell might differ. We confirmed that our RNTs were mainly present in endosomes (Figure 3B). The differences in location possibly alter the measured $\Delta T$ by alternating the

thermal conductivity as discussed in Supporting Information.

By measuring both the temperature and $Ca^{2+}$ dynamics at the same time inside the cell, a positive relationship was found between the temperature increase and the maximum fluorescence intensity of Fluo-4 (Figure 4D). The current results suggest that the amount of heat production we observed is dependent on $Ca^{2+}$ concentration ($[Ca^{2+}]$). We have previously shown that ionomycin-induced heat production is suppressed when cells are pretreated by an inhibitor of the sarco/endoplasmic reticulum $Ca^{2+}$-ATPase (SERCA), thapsigargin.[25] The $Ca^{2+}$ transport coupled with ATP hydrolysis by SERCA is known to mediate heat production in nonshivering thermogenesis in the heater organs of fish[26,27] and mammals.[28,29] On the molecular scale, the efficiency of heat production in SERCA could be increased by the decrease of the $Ca^{2+}$ gradient between the cytosol and the ER lumen.[30] The temperature increase observed here, however, cannot be explained solely by heat production in SERCAs (a difference of ~$10^5$; see Supporting Information for details of this calculation). The elevation of $[Ca^{2+}]$ in the cytosol activates a variety of processes.[17] All of these mechanisms, such as $Ca^{2+}$-regulated active transport by motor proteins,[31] calmodulin-dependent protein kinase II activity,[32] abnormal metabolism at mitochondria, and $Ca^{2+}$-sensitive protein-digesting enzymes that cause irreversible disintegration of cells, probably act as contributing heat sources to the heat production we observed. In the future, the specific contribution of each of these processes should be examined one by one in order to calculate the details of the temperature increase we observed. In addition, the thermodynamic parameters for the cells, which are required for the aforementioned calculation, have not yet been experimentally obtained. According to recent studies on nanoscale heat transfer processes in solid materials, the overall thermal conductivity of the system is significantly reduced due to the boundary conductance when the grain size is taken down to the nanoscale.[33−35] This phenomenon is predicted to exist on liquid−liquid interfaces as well.[36] The cytoplasm is filled with high concentrations of soluble proteins and inner structures with phospholipid bilayers. The average thermal conductivity inside the cell, therefore, might be much smaller than that of water at this scale.

## CONCLUSION

The ratiometric measurement of our RNT demonstrated two benefits in terms of accuracy; one was the environment-independent measurement of the temperature, and the other was the ability of negating the focus drift. These advantages were experimentally demonstrated here at the macroscopic level in a cuvette and at the microscopic level under the optical

microscope. The RNTs moved in *x, y,* and *z* directions in living cells during both the gradual heating and the $Ca^{2+}$ burst. While the temperature change in these situations can hardly be determined from fluorescence intensity, the ratiometric measurement was able to successfully negate the effects of unfocusing, thereby facilitating measurement. Furthermore, each RNT spot successfully measured the temperature as a function of time.

Intracellular local thermodynamics could play a pivotal role in cellular activities relating to the homeostasis of the body temperature and energy balance. In this study, we developed new fluorescent nanoparticles to quantify intracellular temperature. This enabled us to clarify the relationship between the cellular activity and the change in temperature at a subcellular level. The large Stokes shift of Eu-TTA minimizes the influence of autofluorescence that is caused by biological samples illuminated by excitation light shorter than blue. Our RNT may therefore be appropriate for temperature measurements from spheroid cultures, in addition to single cultured cells. *In vivo* thermometry could also be possible by injecting RNTs into the tail vein and imaging them in blood vessels at the surface of exposed organs in live animals.[37] The role of heat in intra- and intercellular signaling, *i.e.*, thermal signaling, could be demonstrated if the endogenous thermogenesis of a single cell could be shown to be coupled with cellular responses such as the activation of heat shock factors in the same cell or other cells. Measuring dynamic heat production in time and space at discrete spots will improve our understanding of chemical reactions in living cells when combined with measurements of cellular parameters such as $[Ca^{2+}]$.

## METHODS

**Materials.** Poly(methyl methacrylate) ($M_w$: 94 600) and poly(allylamine hydrochloride) ($M_w$: 15 000) were purchased from Sigma-Aldrich Co. Europium(III) thenoyltrifluoroacetonate trihydrate was purchased from Acros Organics. Rhodamine 101 inner salt was purchased from Santa Cruz Biotechnology, Inc. Poly(vinyl alcohol) ($M_w$: 15 000) and all organic solvents were purchased from Kanto Chemical.

**Preparation of RNTs.** PMMA (10 mg), Eu-TTA (18 mg), and rhodamine 101 inner salt (0.1 mg) were dissolved in acetone (2 mL). The solution was slowly added to 4 mL of aqueous solution containing poly(vinyl alcohol) (10 mg) and PAH (8 mg) and stirred for 3 h at 1000 rpm at room temperature. The mixed suspension was heated to 50 °C to completely evaporate the acetone. This crude particle suspension was centrifuged (1500*g*, 15 min, 20 °C, MX-305 TOMY) to separate aggregated particles. The supernatant was further purified on a Sephadex PD10 column (GE Healthcare) to remove free polymers and dyes. The primary RNT solution obtained was at a concentration of 1.5 mg/mL including all components estimated from their dried weight.

**Characterization of RNT.** Samples for scanning electron microscopy (SEM) and transmission electron microscopy (TEM) were prepared as a 10-fold dilution of primary RNT solution. They were dropped onto a carbon-coated microgrid (Cu 200 mesh, JEOL) and observed by SEM (Hitachi S-5500, operated at 5.0 kV) and TEM (Hitachi H-7650, operated at 100 kV). All SEM samples were processed with Pt−Pd ion sputtering for five seconds (E-1030, Hitachi). Samples for atomic force microscopy (AFM) were prepared as a mixture of primary RNT solution (20 $\mu$L) and L-15 medium (1 mL) [Leibovitz's $CO_2$-independent medium without phenol red (Gibco) supplemented with 10% fetal bovine serum (Gibco)]. After 30 min of incubation in a glass-based dish (Φ 35 mm, Iwaki) followed by washing away of unattached RNTs with deionized water (Milli-Q, Millipore), the dried coverslip was observed by AFM (VN-8000, Keyence). The characteristics of RNTs in subaqueous conditions were determined by dynamic light scattering (DLS) and laser Doppler velocimetry (LDV) with a Malvern Zetasizer Nano ZS. The primary RNT solution was diluted 100-fold with either phosphate-buffered saline (PBS) solution (10 mM phosphate buffer, 150 mM KCl, pH 7.4), DMEM (Invitrogen) for DLS, or deionized water for LDV.

**Evaluation of Fluorescence Properties under Various Conditions.** Fluorescence spectra of RNTs were recorded by a spectrophotometer (RF5300PC, Shimadzu) at every 2 °C increase from 26 to 40 °C with an accuracy of ±0.1 °C. The primary RNT solution was diluted 1000-fold with PBS in a 10 mm thick quartz cell.

Eu-TTA and rhodamine 101 were excited at 340 and 530 nm, respectively. The slit width was 5 nm. The temperature of the RNT solution was controlled by a thermostat bath (BU150A, Yamato) and measured with a digital thermocouple (ASF-250T, AS ONE) to an accuracy of ±0.1 °C. Sensitivity to pH, ionic strength, protein concentration, and viscosity was measured by Power Scan (DS Pharma Biomedical). Eu-TTA was excited at 360 ± 20 nm, and the fluorescence was collected at 590 ± 35 nm. Rhodamine 101 was excited at 530 ± 40 nm, and the fluorescence was collected at 590 ± 35 nm. The fluorescence ratio was calculated from the total fluorescence in each well. The pH of PBS (pH 4.0−10.0) was adjusted using HCl or KOH as monitored by a pH meter (F-52, Horiba). Ionic strength and protein concentration were regulated by KCl (0−500 mM) and bovine serum albumin (BSA, Sigma-Aldrich Co.) (0−45 wt %), respectively. Viscosity (1−220 cP) was adjusted using glycerol (0−92 wt % glycerol/PBS) and calculated at 25 °C.[38] The RNT solution was diluted 100-fold into each of these buffers in a 96-well plate. The temperature of the 96-well plate was set by a built-in incubator. Thermal sensitivity in various conditions was measured using a RF5300PC by the same method described above for the measurement of the thermosensitive spectra of RNTs in PBS.

**Reversibility of the Temperature-Dependent Fluorescence Ratio.** RNTs were diluted 1000 times in PBS, and the fluorescence spectra were measured using a RF5300PC spectrofluorophotometer as described in Evaluation of Fluorescence Properties under Various Conditions. The temperature was alternately changed five times between 30 and 40 °C.

**Stability in Various Oxygen Concentrations.** Fluorescence spectra were measured by a RF5300PC spectrofluorophotometer at 28 °C as described in Evaluation of Fluorescence Properties under Various Conditions. Primary RNT solution was diluted 1000-fold in PBS. The cuvette was sealed, and the fluorescence spectra were measured at the ambient condition. For the lower oxygen level condition, the solution was bubbled with nitrogen gas for 2 min and the fluorescence spectra were measured. The solution was then bubbled with oxygen gas for 2 min, and the fluorescence spectra were measured at a higher oxygen level. Finally, the sealed cuvette was released and the fluorescence spectra were measured after 5 min at the ambient condition.

**Temporal Stability in Phosphate Buffer.** Primary RNT solution was diluted 100-fold in either deionized water or PBS. The fluorescence ratio was measured at 0, 2, 4, 12, and 24 h by Power Scan at 28 °C. The scanning setup was the same as that described in Evaluation of Fluorescence Properties under Various Conditions.

**Cell Culture.** HeLa cells were cultured on glass-based dishes in culture medium [89% DMEM (Invitrogen) containing 10%

fetal bovine serum (Invitrogen) and 1% penicillin−streptomycin (Invitrogen)] at 37 °C in the presence of 5% $CO_2$.

**Loading of RNTs into Cells.** Primary RNT solution (20 $\mu$L) was dispersed onto cells in culture medium (2 mL) and incubated for 2 h at 37 °C in the presence of 5% $CO_2$. The cells in the culture medium were then washed with PBS and placed into L-15 medium.

**Cell Viability Test.** HeLa cells were seeded onto a 96-well plate with a density of $5 \times 10^4$ cells/mL (90 $\mu$L/well) and cultured for 12 h in culture medium at 37 °C in the presence of 5% $CO_2$. After removal of the culture medium, 10 $\mu$L of RNT solution (15−0.0045 mg/mL) and 90 $\mu$L of culture medium were added to each well and incubated for 2 h. After washing with PBS (2 × 100 $\mu$L), 100 $\mu$L of culture medium and 10 $\mu$L of Cell Counting Kit-8 solution (Dojindo Laboratories, Japan) were added to each well and incubated for an additional 2 h. The absorbance values at 450 nm for each well were determined using a microplate reader.

**Confocal Imaging of RNTs in HeLa Cells Labeled by Organelle Tracking Dyes.** Cells were incubated with RNTs and either 5 $\mu$g/mL of Dextran Cascade Blue 3000 $M_w$ (Invitrogen) for visualizing endosomes or 100 nM LysoTracker (Invitrogen) for visualizing lysosomes in culture medium for 2 h at 37 °C in the presence of 5% $CO_2$. The medium was replaced by L-15 medium and observed under a confocal fluorescence microscope (FV1000, Olympus) at 37 °C (INUB-ONICS, Tokai Hit). The Golgi apparatus of RNT-preloaded HeLa cells was stained with NBD C6 ceramide solution. Mitochondria and endoplasmic reticulum of RNT-preloaded HeLa cells were stained with 2.5 nM Mito Fluor far red (Invitrogen) and 500 nM of ER-Tracker Green (Invitrogen), respectively.

**Properties of RNTs under the Optical Microscope.** Primary RNT solution (20 $\mu$L) was dispersed in 1 mL of L-15 medium [Leibovitz's $CO_2$-independent medium without phenol red (Gibco) supplemented with 10% fetal bovine serum (Gibco)] in glass-based dishes (Φ 35 mm, Iwaki) and kept at room temperature for 30 min. The particles spontaneously attached to the glass surface. Single RNT spots were imaged using an oil immersion objective (PlanApoN 60XO, Olympus) under an inverted microscope equipped with an autofocusing unit (IX81-ZDC, Olympus). Eu-TTA and rhodamine 101 in RNTs were excited by a mercury lamp through excitation filters FF01-360/12 (Semrock) and BP535-555HQ (Olympus), dichroic mirrors FF409-Di03 (Semrock) and DM565HQ (Olympus), and emission filters FF01-629/56 (Semrock) and BA570-625HQ (Olympus), respectively, and imaged with a cooled CCD camera (CoolSNAP HQ2, Photometrics). The temperature of the sample was controlled by a stage top incubator equipped with four types of heaters (top cover, stage, water bath, and lens heaters) and feedback from a thermocouple (INUCP-KRi, Tokai Hit). The thermocouple monitored the actual temperature of the medium. The effect of photobleaching on the fluorescence intensity was measured at 28 °C. The fluorescence intensity of single spots was measured each time they were excited (20 times). The periods of exposure were 10 and 100 ms for Eu-TTA and rhodamine 101, respectively. The photobleaching behavior of Eu-TTA and rhodamine 101 in an RNT spot was measured separately (Figure S6), and they were applied for single spot analysis in Figures 3D−G, S7, and S8. When determining the relationship between the temperature and the fluorescence ratio, the temperature of the medium was gradually increased by 1 °C increments from 34 to 40 °C (at the rate of ~0.2 °C/min) (Figure 3C−G and Figure S7). The ratio value did show a distribution at each temperature (Figure S7A); however the distribution was reduced when the threshold for the fluorescence intensity was reached (Figure S7B). Only the RNT spots brighter than this threshold were analyzed in single-spot measurements (Figures 3 and S7C). The influence of the position along the z-axis on both the fluorescence intensity of Eu-TTA and rhodamine 101 and the ratio was measured by moving the objective lens stepwise by steps of 200 nm across the glass surface at 28 °C.

**Intracellular Heat Production Induced by $Ca^{2+}$ Ionophore.** The culture medium containing HeLa cells, which were loaded with RNTs, was replaced with L-15 medium without FBS. Then, 1 $\mu$L of 1 mM Fluo-4 AM (Invitrogen) in DMSO was added to 1 mL of medium, resulting in a final concentration of 1 $\mu$M. After

incubation for 30 min at 37 °C, the medium was replaced with L-15 medium including FBS. Eu-TTA, rhodamine 101, and Fluo-4 were excited for 20, 100, and 100 ms, respectively, in this order, and a differential interference contrast microscopy image was captured every 10 s for 200 s (21 times). A BP460-480HQ excitation filter, a DM485 dichroic mirror, and a BA495-540HQ emission filter (all from Olympus) were used for the imaging of Fluo-4. In between t = 50 and 60 s, 20 $\mu$L of 200 $\mu$M ionomycin in PBS (diluted from 2 mM stock in DMSO to DMSO/PBS = 1:9) was added from one side of the dish (Φ 35 mm) to a final concentration of 4 $\mu$M. In control measurements, 20 $\mu$L of DMSO solution (DMSO/PBS = 1:9) without ionomycin was added to the dish.

**Data Analysis.** All fluorescence images of RNTs obtained under the fluorescence microscope were analyzed using ImageJ software. Each RNT spot was surrounded by a circular region of interest (ROI), and the fluorescence intensity of the whole region was obtained. The background was determined for each spot. The size and shape of the ROI for the background was the same as that used for the spot. The ROI for the background was placed next to the spot of interest. The total intensity of the background ROI was subtracted from the whole fluorescence intensity to obtain the actual fluorescence intensity of the RNT spot. In determining the relationship between the temperature and the fluorescence ratio, the spot was not analyzed when its xy-position was displaced during the automatic exchange of the filter set at ~2 s (Figures 3C−G and S7 and Movie S1). In the measurements using ionomycin-stimulated HeLa cells, the location of the ROI was refreshed every camera frame to track the same spot of interest throughout the entirety of the movie (Figures 4, S9, and S10 and Movie S2).

*Conflict of Interest:* The authors declare no competing financial interest.

*Supporting Information Available:* TEM, SEM, and AFM images of RNTs, size distributions of RNTs, and fluorescence spectra of Eu-TTA and rhodamine 101 in RNTs (Figures S1 and S2); additional data determined in a cuvette (Figures S3 and S4); cytotoxicity test (Figure S5); additional data determined by single RNT spots under the optical microscope (Figures S6−S10); movies of a cell and RNTs captured under the optical microscope (Movies S1 and S2); additional table (Table S1). This material is available free of charge via the Internet at http://pubs.acs.org.

## REFERENCES AND NOTES

1. Brites, C. D.; Lima, P. P.; Silva, N. J.; Millan, A.; Amaral, V. S.; Palacio, F.; Carlos, L. D. Thermometry at the Nanoscale. *Nanoscale* **2012**, *4*, 4799–4829.

2. Ozawa, T.; Yoshimura, H.; Kim, S. B. Advances in Fluorescence and Bioluminescence Imaging. *Anal. Chem.* **2013**, *85*, 590–609.

3. Albers, A. E.; Chan, E. M.; McBride, P. M.; Ajo-Franklin, C. M.; Cohen, B. E.; Helms, B. A. Dual-Emitting Quantum Dot/ Quantum Rod-Based Nanothermometers with Enhanced Response and Sensitivity in Live Cells. *J. Am. Chem. Soc.* **2012**, *134*, 9565–9568.

4. Yang, J. M.; Yang, H.; Lin, L. Quantum Dot Nano Thermometers Reveal Heterogeneous Local Thermogenesis in Living Cells. *ACS Nano* **2011**, *5*, 5067–5071.

5. Hsia, C. H.; Wuttig, A.; Yang, H. An Accessible Approach to Preparing Water-Soluble $Mn^{2+}$-Doped (CdSSe)Zns (Core)-Shell Nanocrystals for Ratiometric Temperature Sensing. *ACS Nano* **2011**, *5*, 9511–9522.

6. Donner, J. S.; Thompson, S. A.; Kreuzer, M. P.; Baffou, G.; Quidant, R. Mapping Intracellular Temperature Using Green Fluorescent Protein. *Nano Lett.* **2012**, *12*, 2107–2111.

7. Vetrone, F.; Naccache, R.; Zamarron, A.; Juarranz de la Fuente, A.; Sanz-Rodriguez, F.; Martinez Maestro, L.; Martin Rodriguez, E.; Jaque, D.; Garcia Sole, J.; Capobianco, J. A. Temperature Sensing Using Fluorescent Nanothermometers. *ACS Nano* **2010**, *4*, 3254–3258.

8. Fischer, L. H.; Harms, G. S.; Wolfbeis, O. S. Upconverting Nanoparticles for Nanoscale Thermometry. *Angew. Chem., Int. Ed.* **2011**, *50*, 4546–4551.

9. Ye, F.; Wu, C.; Jin, Y.; Chan, Y. H.; Zhang, X.; Chiu, D. T. Ratiometric Temperature Sensing with Semiconducting Polymer Dots. *J. Am. Chem. Soc.* **2011**, *133*, 8146–8149.

10. Gota, C.; Okabe, K.; Funatsu, T.; Harada, Y.; Uchiyama, S. Hydrophilic Fluorescent Nanogel Thermometer for Intracellular Thermometry. *J. Am. Chem. Soc.* **2009**, *131*, 2766–2767.

11. Okabe, K.; Inada, N.; Gota, C.; Harada, Y.; Funatsu, T.; Uchiyama, S. Intracellular Temperature Mapping with a Fluorescent Polymeric Thermometer and Fluorescence Lifetime Imaging Microscopy. *Nat. Commun.* **2012**, *3*, 705.

12. Peng, H.-S.; Huang, S.-H.; Wolfbeis, O. S. Ratiometric Fluorescent Nanoparticles for Sensing Temperature. *J. Nanopart. Res.* **2010**, *12*, 2729–2733.

13. Brites, C. D.; Lima, P. P.; Silva, N. J.; Millan, A.; Amaral, V. S.; Palacio, F.; Carlos, L. D. A Luminescent Molecular Thermometer for Long-Term Absolute Temperature Measurements at the Nanoscale. *Adv. Mater.* **2010**, *22*, 4499–4504.

14. Brites, C. D.; Lima, P. P.; Silva, N. J.; Millan, A.; Amaral, V. S.; Palacio, F.; Carlos, L. D. Lanthanide-Based Luminescent Molecular Thermometers. *New J. Chem.* **2011**, *35*, 1177–1183.

15. Peng, H.; Stich, M. I.; Yu, J.; Sun, L. N.; Fischer, L. H.; Wolfbeis, O. S. Luminescent Europium(Iii) Nanoparticles for Sensing and Imaging of Temperature in the Physiological Range. *Adv. Mater.* **2010**, *22*, 716–719.

16. Oyama, K.; Takabayashi, M.; Takei, Y.; Arai, S.; Takeoka, S.; Ishiwata, S.; Suzuki, M. Walking Nanothermometers: Spatiotemporal Temperature Measurement of Transported Acidic Organelles in Single Living Cells. *Lab Chip* **2012**, *12*, 1591–1593.

17. Berridge, M. J.; Bootman, M. D.; Lipp, P. Calcium—a Life and Death Signal. *Nature* **1998**, *395*, 645–648.

18. Ahlin, P.; Kristl, J.; Kristl, A.; Vrecer, F. Investigation of Polymeric Nanoparticles as Carriers of Enalaprilat for Oral Administration. *Int. J. Pharm.* **2002**, *239*, 113–120.

19. Ohtsuka, K.; Sato, S.; Sato, Y.; Sota, K.; Ohzawa, S.; Matsuda, T.; Takemoto, K.; Takamune, N.; Juskowiak, B.; Nagai, T.; *et al.* Fluorescence Imaging of Potassium Ions in Living Cells Using a Fluorescent Probe Based on a Thrombin Binding Aptamer-Peptide Conjugate. *Chem. Commun.* **2012**, *48*, 4740–4742.

20. Bright, G. R.; Fisher, G. W.; Rogowska, J.; Taylor, D. L. Fluorescence Ratio Imaging Microscopy: Temporal and Spatial Measurements of Cytoplasmic pH. *J. Cell. Biol.* **1987**, *104*, 1019–1033.

21. Modi, S.; M, G. S.; Goswami, D.; Gupta, G. D.; Mayor, S.; Krishnan, Y. A DNA Nanomachine That Maps Spatial and Temporal Ph Changes inside Living Cells. *Nat. Nanotechnol.* **2009**, *4*, 325–330.

22. Llopis, J.; McCaffery, J. M.; Miyawaki, A.; Farquhar, M. G.; Tsien, R. Y. Measurement of Cytosolic, Mitochondrial, and Golgi Ph in Single Living Cells with Green Fluorescent Proteins. *Proc. Natl. Acad. Sci. U.S.A.* **1998**, *95*, 6803–6808.

23. Kuimova, M. K.; Botchway, S. W.; Parker, A. W.; Balaz, M.; Collins, H. A.; Anderson, H. L.; Suhling, K.; Ogilby, P. R. Imaging Intracellular Viscosity of a Single Cell during Photoinduced Cell Death. *Nat. Chem.* **2009**, *1*, 69–73.

24. Wang, L.; Xiao, Y.; Tian, W.; Deng, L. Activatable Rotor for Quantifying Lysosomal Viscosity in Living Cells. *J. Am. Chem. Soc.* **2013**, *135*, 2903–2906.

25. Suzuki, M.; Tseeb, V.; Oyama, K.; Ishiwata, S. Microscopic Detection of Thermogenesis in a Single Hela Cell. *Biophys. J.* **2007**, *92*, L46–L48.

26. Block, B. A.; Franzini-Armstrong, C. The Structure of the Membrane Systems in a Novel Muscle Cell Modified for Heat Production. *J. Cell Biol.* **1988**, *107*, 1099–1112.

27. Block, B. A.; O'Brien, J.; Meissner, G. Characterization of the Sarcoplasmic Reticulum Proteins in the Thermogenic Muscles of Fish. *J. Cell Biol.* **1994**, *127*, 1275–1287.

28. MacLennan, D. H. $Ca^{2+}$ Signalling and Muscle Disease. *Eur. J. Biochem.* **2000**, *267*, 5291–5297.

29. Bal, N. C.; Maurya, S. K.; Sopariwala, D. H.; Sahoo, S. K.; Gupta, S. C.; Shaikh, S. A.; Pant, M.; Rowland, L. A.; Bombardier, E.; Goonasekera, S. A.; *et al.* Sarcolipin Is a Newly Identified Regulator of Muscle-Based Thermogenesis in Mammals. *Nat. Med.* **2012**, *18*, 1575–1579.

30. de Meis, L.; Arruda, A. P.; Carvalho, D. P. Role of Sarco/Endoplasmic Reticulum Ca(2+)-Atpase in Thermogenesis. *Biosci. Rep.* **2005**, *25*, 181–190.

31. Wang, X.; Schwarz, T. L. The Mechanism of $Ca^{2+}$-Dependent Regulation of Kinesin-Mediated Mitochondrial Motility. *Cell* **2009**, *136*, 163–174.

32. De Koninck, P.; Schulman, H. Sensitivity of Cam Kinase II to the Frequency of $Ca^{2+}$ Oscillations. *Science* **1998**, *279*, 227–230.

33. Cahill, D. G.; Goodson, K.; Majumdar, A. Thermometry and Thermal Transport in Micro/Nanoscale Solid-State Devices and Structures. *J. Heat Transfer* **2002**, *124*, 223–241.

34. Yang, H.-S.; Bai, G. R.; Thompson, L. J.; Eastman, J. A. Interfacial Thermal Resistance in Nanocrystalline Yttria-Stabilized Zirconia. *Acta Mater.* **2002**, *50*, 2309–2317.

35. Angadi, M. A.; Watanabe, T.; Bodapati, A.; Xiao, X.; Auciello, O.; Carlisle, J. A.; Eastman, J. A.; Keblinski, P.; Schelling, P. K.; Phillpot, S. R. Thermal Transport and Grain Boundary Conductance in Ultrananocrystalline Diamond Thin Films. *J. Appl. Phys.* **2006**, *99*, 114301.

36. Patel, H. A.; Garde, S.; Keblinski, P. Thermal Resistance of Nanoscopic Liquid-Liquid Interfaces: Dependence on Chemistry and Molecular Architecture. *Nano Lett.* **2005**, *5*, 2225–2231.

37. Gonda, K.; Watanabe, T. M.; Ohuchi, N.; Higuchi, H. In Vivo Nano-Imaging of Membrane Dynamics in Metastatic Tumor Cells Using Quantum Dots. *J. Biol. Chem.* **2010**, *285*, 2750–2757.

38. Sheely, M. L. Glycerol Viscosity Tables. *Ind. Eng. Chem.* **1932**, *24*, 1060–1064.